

A Capacitive Ice Detection Microsensor

Shuvo Roy*, Russell G. DeAnna**, Mehran Mehregany and Eugene Zakar¹

Microfabrication Laboratory, Department of Electrical Engineering and Computer Science
Case Western Reserve University, Cleveland, OH 44106, USA

¹US Army Research Lab., Adelphi, MD 20783-1197, USA

(Received December 7, 1998; accepted February 7, 2000)

Key words: ice detection, capacitance sensor, icing, microsensors, ice properties

An ice detection system using a microfabricated diaphragm as the sensing element and portable capacitance detection circuitry is presented. During operation, actuation forces are applied electrostatically to cause diaphragm deformation. Accumulation of ice on the diaphragm leads to an increase in its effective stiffness. Therefore, for a given actuation voltage, the ice-covered diaphragm exhibits a smaller deflection than the corresponding ice-free diaphragm. This deflection is measured using a customized, portable, high-sensitivity, differential capacitance measurement circuit. Finite-element analysis (FEA) is used to optimize the sensor geometry for enhanced sensitivity to ice accretion. The sensor is fabricated by bulk micromachining and wafer bonding of silicon and glass substrates. The sensor is operated with the diaphragm in the stiffness-sensitive mode, enabling the discrimination between ice and water (or deicing fluids) films. Calibration experiments reveal that the miniature ice detection sensor system can successfully detect ice and water film thicknesses between approximately 0.5–1.5 mm. Finally, dynamic testing indicates that the adhesion of ice to silicon is poor when the sensor is driven continuously.

1. Introduction

Aircraft ice detection systems have received a great deal of attention because of their importance in flight safety. In-flight icing is caused by the presence of metastable, super-cooled, water droplets in clouds usually between -10°C to 0°C .^(1,2) When the aircraft encounters these droplets, they may either suddenly change phase from liquid to solid upon impact, or they may impact and flow back as a thin film of water, collect into

* Presently at Department of Biomedical Engineering, The Cleveland Clinic Foundation, Cleveland, Ohio 44195, USA.

**Army Research Laboratory, NASA Glenn Research Center, Cleveland, Ohio 44135, USA.

droplets due to surface tension, and then freeze.⁽³⁾ The buildup of ice on the leading edges of fixed wings causes an increase in drag and a decrease in the lift of the aircraft.^(3,4) Ice formation can also result in the inability to retract moveable surfaces, such as slats and flaps. Furthermore, dislodged ice can damage the aircraft skin, antennae or other instrumentation, and cause catastrophic engine failure if sucked in. These potentially severe problems have led to the need for reliable and robust sensors for the detection of ice.

Conventional aircraft ice detection technology relies on macroscale sensors that often require elaborate assembly, handling, and installation procedures.^(4,5) Furthermore, sensor geometry and placement orientations may adversely affect local airflow during aircraft operation. In contrast, a flush-mounted sensor system based on micro-electromechanical systems (MEMS) technology, which has the inherent advantages of smaller size and microelectronics compatibility, is particularly attractive for ice detection.⁽⁶⁾ This study is an extension of previous work and details the development of a miniature system for ice detection using a microfabricated diaphragm as the sensing element and portable capacitance detection circuitry.^(6,7) First, a suitable sensor design to enable flush-mounting is selected and analyzed for feasibility. Next, the device is fabricated by bulk micromachining and wafer bonding of glass and silicon substrates. The microfabricated diaphragm is appropriately packaged to ensure faithful operation upon exposure to icing conditions. Also, sensor interface circuitry is built on a printed wiring board (PWB) using discrete, low-power, commercially available components. Finally, the ice detection sensor is tested by loading the diaphragm under various temperature/phase conditions and monitoring the output of the interface circuitry.

2. Design

Figure 1 is a schematic showing the general design concept of the ice detection sensor. A p+ silicon membrane is suspended above, and electrically isolated from, the lower electrodes. When a voltage is applied between the actuation electrode and the diaphragm, attractive electrostatic forces cause the diaphragm to deform downward toward the sense electrode, increasing the capacitance between the sense electrode and the diaphragm. Accumulation of ice across the diaphragm and its anchor regions leads to an increase in effective diaphragm stiffness. Therefore, for a given actuation voltage, the ice-covered diaphragm exhibits a smaller deflection than a corresponding ice-free diaphragm.

2.1 Finite-element modeling

The sensor structure is modeled using finite-element analysis to determine the feasibility of the proposed design concept and possible optimization. In order to gain insight into diaphragm behavior under different conditions, "worst-case" scenarios are examined using ANSYS with a four-node, layered shell element meshing, which allows for simulation of multilayered membrane structures. A one-quarter symmetry model of a square silicon diaphragm of 1 mm side by 10- μ m-thick (Layer 1) and a 100- μ m-thick ice film (Layer 2) is used. Symmetry boundary conditions are applied on the two center edges and fixed boundary conditions on the two outside edges. The one-quarter symmetry model

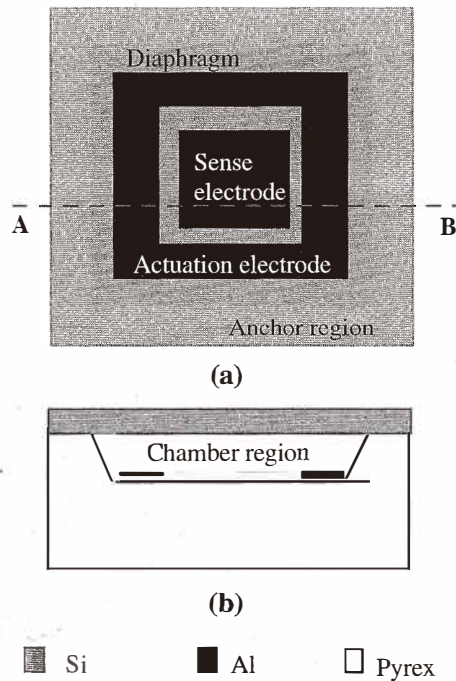


Fig. 1. Design concept of microfabricated ice detection sensor using a p+ silicon membrane: (a) plan thru-view; and (b) cross section across dashed line AB.

area is meshed by 400 (20×20) elements. The applied electrostatic actuation, corresponding to an actuation voltage of approximately 50 V, is simulated as a pressure on the membrane area. Using a parallel-plate capacitor model, the electrostatic pressure, P , for a given actuation voltage, V , is given by:

$$P = \frac{\epsilon V^2}{2x^2}, \quad (1)$$

where ϵ is the permittivity of air, 8.85×10^{-12} F/m, and x is the original gap space, 2×10^{-6} m. The presence of water on the diaphragm is simulated by the application of an additional pressure, corresponding to the weight of the water film, on the membrane. Table 1 presents the material properties used for the model.^(8,9)

Table 1
Material properties for FEA.

	Si	Ice
Young's modulus (GPa)	160	10
Density (kg/m ³)	2330	980
Poisson's ratio	0.25	0.25

The FEA results for diaphragm deflection are shown in Fig. 2. The ice-free diaphragm exhibits a center deflection of approximately $0.25 \mu\text{m}$ under electrostatic actuation (Fig. 2(a)). In the case of water films, the weight of a 10-mm-thick water layer on the diaphragm leads to a $0.04 \mu\text{m}$ center deflection (Fig. 2(b)). Under electrostatic actuation, the water-covered diaphragm exhibits a $0.29 \mu\text{m}$ deflection at the center. These results suggest that the presence of water on the diaphragm has a minimal, and possibly negligible, effect on diaphragm deflection characteristics.

When covered by a $100\text{-}\mu\text{m}$ -thick ice film, the diaphragm's center deflection decreases to $0.001 \mu\text{m}$ under electrostatic actuation (Fig. 2(c)). Thus, the stiffening effect of ice on diaphragm deflection is significantly greater than that due to its weight. Figure 3 presents the von Mises stress distribution on the ice-free diaphragm under electrostatic

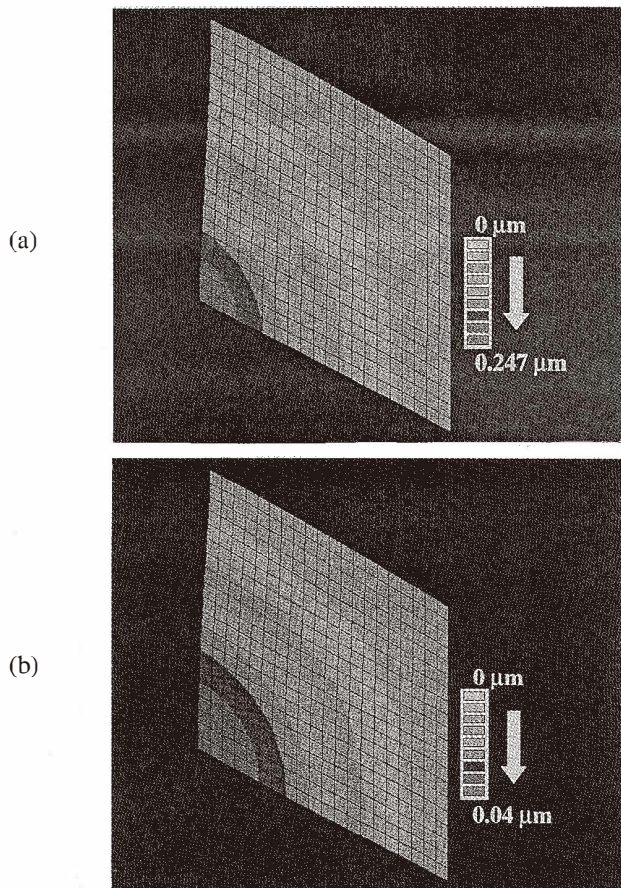


Fig. 2. FEA results showing diaphragm deflection under various conditions: (a) ice/water-free diaphragm with 50 V electrostatic actuation; (b) 10-mm-thick water layer only.

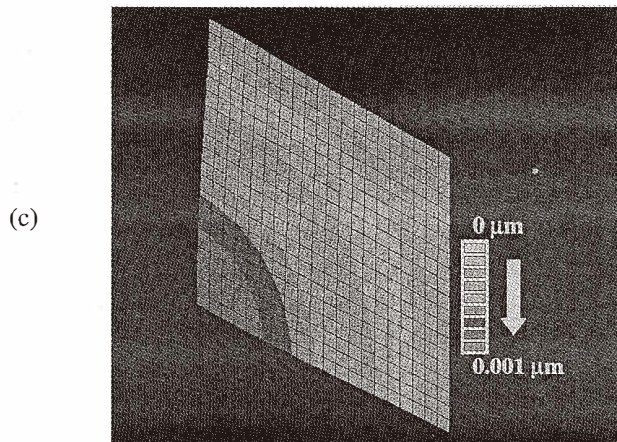


Fig. 2. FEA results showing diaphragm deflection under various conditions: (c) 100- μm -thick ice layer with 50 V electrostatic actuation.

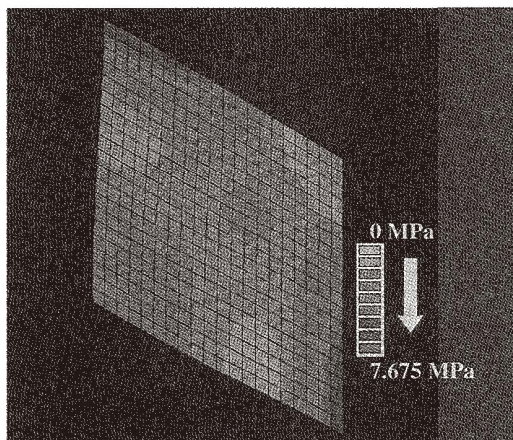


Fig. 3. FEA model of von Mises stress distribution on sensor diaphragm. The maximum stress regions are located at the centers of the diaphragm edges.

actuation. The maximum stress regions are located at the centers of the diaphragm edges, while the corner regions exhibit much lower stress values. The maximum stress value of approximately 7.7 MPa is well below the yield strength of silicon, thereby ensuring a repeatable diaphragm characteristic for successive actuation cycles.⁽⁸⁾

The effect of compressive residual stresses, which are reported to originate during the fabrication of p+ diaphragms, is also examined.^(10,11) Compressive residual stress in the

silicon diaphragm is simulated by applying a pressure load, corresponding to the residual stress, to the two outside area edges, and enabling in-plane displacement of those edges. The center deflection of the ice-free diaphragm with a 74 MPa compressive residual stress under the 50 V electrostatic load is 0.50 μm (compared to 0.25 μm with no residual stress). The increased deflection is due to stress softening. The 74 MPa compressive stress is selected for the model because it represents the minimum theoretical Euler buckling load for the diaphragm. For a square membrane, the Euler buckling load is given by:⁽¹²⁾

$$\sigma_{critical} = \frac{16\pi^2 D}{3ha^2}, \quad (2)$$

where $D = Eh^3/12(1-\nu^2)$ denotes the flexural rigidity of the membrane of thickness h , edge length a , Young's modulus E , and Poisson's ratio ν . The first three buckled mode shapes and corresponding Euler buckling loads are shown in Fig. 4. A more accurate estimate of the minimum buckling load is obtained by performing a nonlinear buckling analysis using ANSYS. This analysis reveals that the minimum buckling load for the square diaphragm is 68 MPa.

2.2 Packaging issues

The sensor structure and measurement system should be sensitive and robust to ensure faithful operation upon exposure to icing conditions. Typically, a larger diaphragm exhibits greater capacitance, deflection, and sensitivity. However, the larger diaphragm tends to be less robust mechanically and more sensitive to vibrations and fluctuations in air pressure. The detection of ice is accomplished by monitoring capacitance change as a function of applied electrostatic actuation. Therefore, these capacitance change measurements should be insensitive to environmental conditions. Also, moisture accumulation should be prevented in the diaphragm chamber region; otherwise, electrode corrosion will occur, and the high dielectric constant of water will lead to erroneously large capacitance changes.

In order to address the packaging issues described above, the sensor design includes air-release channels between the chamber region and external ambient. These channels allow the equilibration of pressure on both sides of the diaphragm, thereby ensuring that the sensor is insensitive to ambient pressure. Furthermore, air-release channels prevent any increase in the effective diaphragm stiffness that might result from compression and/or expansion of air inside a sealed chamber volume. In order to ensure that moisture does not seep into the chamber region, the external ports of the air-release channels should be sealed watertight.

In the sensor layout, the air-release channels and electrical interconnects from sensor bond pads to the chamber region are designed to pass under the diaphragm corner regions (see Fig. 6). The stress distribution at these corner regions is relatively low, and therefore, the validity of the FEA deflection models is maintained.

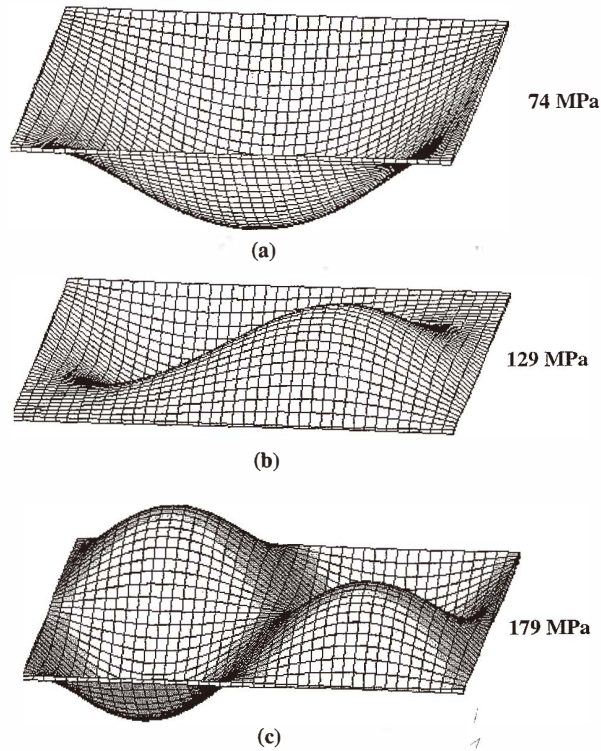


Fig. 4. FEA results showing the first three buckled mode shapes and the corresponding stress load required: (a) first mode; (b) second mode; and (c) third mode.

3. Fabrication and Packaging

The sensor is fabricated by bulk micromachining and wafer bonding of silicon to glass (Pyrex) substrates, as illustrated in Fig. 5. The fabrication process requires two masks associated with two photolithography steps. Starting with the Pyrex substrate, the first mask is used to pattern the shallow recessed area which will eventually form the air gap between the diaphragm and electrodes, air-release channels, and access passages for interconnects. Standard positive resist lithography and HF etchant are used to create the 4- μm -deep recess. Next, a 5,000 Å aluminum layer is deposited on the substrate by sputtering. The electrodes, interconnects, and bond pads are patterned using the second mask, standard lithography and a wet aluminum etch. The isotropic nature of the wet etch ensures the removal of aluminum at the bottom edges of the recessed areas where the aluminum film is thicker than the nominal deposition thickness.

Meanwhile, a (100), n-type, double-sided-polished, silicon wafer with a $\langle 110 \rangle$ major flat is thermally oxidized to grow a 1- μm -thick layer. The oxide on one surface is protected with hard-baked photoresist, while the oxide on the opposite side is removed by

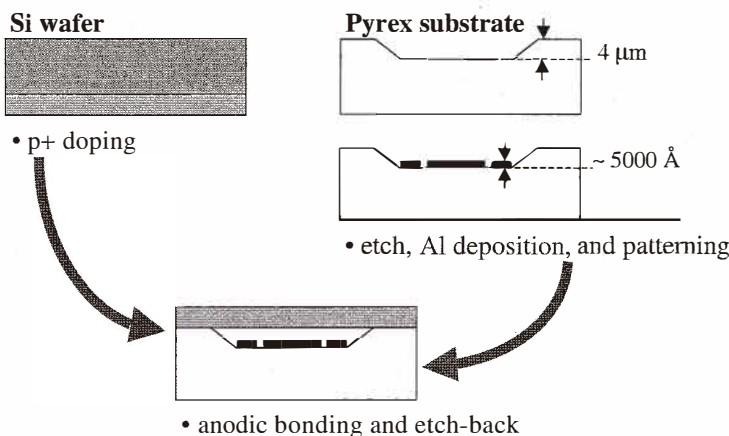


Fig. 5. Schematic illustration of sensor fabrication using a two-mask process.

immersion in buffered HF. Next, the wafer is diffused with boron to create a $7\text{-}\mu\text{m}$ -thick p+ etch stop layer on the bare silicon side. The associated boron-doped glass and the oxide on the opposite surface are removed by immersion in buffered HF.

The doped silicon surface is electrostatically bonded to the patterned Pyrex wafer. This bonding step requires good global alignment of the two wafers, which is accomplished manually with relative ease. The wafer is then etched in ethylene-diamine and pyrocatechol (EDP) to realize a p+ diaphragm anchored to the Pyrex substrate. Close examination revealed that the p+ diaphragm buckled, an effect reported previously in the literature,^(10,11) however, the diaphragm buckled in an irregular and wrinkled shape that did not permit accurate measurement of the diaphragm profile. Nevertheless, sensor operation should still be possible for those diaphragms that are still electrically isolated from the underlying electrodes. The sensor bond pads are exposed by simply breaking away their corresponding diaphragms with a small vacuum probe. The wafer is diced, and the sensor is mounted onto a ceramic carrier substrate using a room-temperature-vulcanizing (RTV) elastomer. Bond wires are then connected between the sensor bond pads and gold leads, which are patterned on the ceramic substrate. Figure 6 presents a schematic of a final packaged sensor. The bonding wires are protected from mechanical loads and environmental exposure using epoxy, which also covers the air-release channel ports and electrode access passages.

4. Experimental Results

4.1 Test setup

Figure 7 presents the test setup used to characterize the ice detection sensor. A packaged sensor is placed on an aluminum block mounted on the cold side of a thermoelectric cooler. The hot side of the cooler is fixed to a copper-plated heat exchanger. The

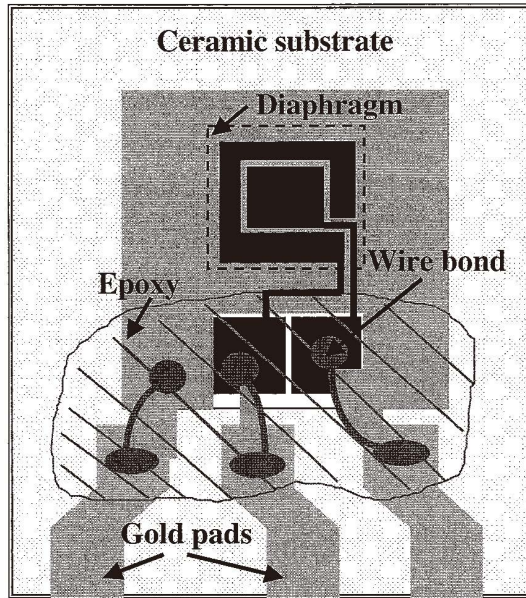


Fig. 6. Plan through-view of the final sensor package. The epoxy protects the bond wires and seals the chamber region watertight from the ambient.

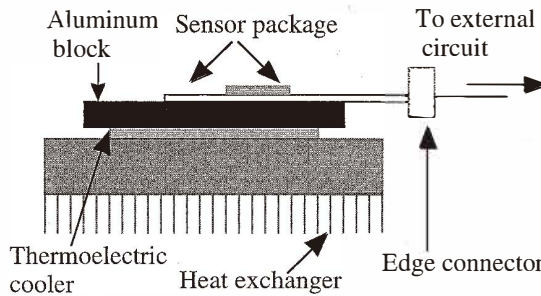


Fig. 7. Experimental setup for testing the operation of ice detection sensor. The external circuit connects to the capacitance measurement circuit.

efficiency of this heat pump is enhanced by using thermal cement at the mounts and fixture regions. Furthermore, the heat exchanger is placed in a 22°C running-water bath, and thermal insulation is used on the cold side to minimize parasitic heat transfer from the ambient. Using these enhancements, the thermoelectric cooler is capable of maintaining a cold-side temperature as low as -20°C, measured using a thermocouple inserted into the aluminum block. It is also possible to convert the system into a heater by changing the direction of the current to the thermoelectric element.

The sense electrode of the ice detection sensor is connected via an edge connector to an external capacitance measurement circuit shown in Fig. 8. This sensor interface circuitry is implemented on a printed wiring board (PWB) using discrete, low-power, commercially available components. In this circuit, the diaphragm and sense electrode constitute a variable capacitor, C_{SENS} . The differential capacitance, ΔC , between C_{SENS} and a known variable capacitor, C_{REF} , is converted to an output voltage, V_o . Using known values of C_{SENS} and C_{REF} , V_o is calibrated in terms of ΔC . The minimum differential capacitance measurable by this circuit, ΔC_{MIN} , is 0.2 pF.

4.2 Results

Prior to testing the microfabricated ice detection sensor under different conditions, the nominal sensor capacitance is determined using a precision capacitance meter. For a sensor with a $1.5 \times 0.6 \text{ mm}^2$ sense electrode and a $2.0 \times 1.0 \text{ mm}^2$ diaphragm, the nominal capacitance of the packaged sensor is measured to be approximately 4 pF, which comprises both sensor and parasitic capacitances. The buckled/wrinkled shape of the diaphragm does not allow for an accurate determination of the sensor capacitance alone. The sealing quality of the epoxy film is also investigated. A layer of water, approximately 1 mm thick is deposited on the epoxy film, epoxy-silicon boundary, and epoxy-ceramic boundary regions of the sensor package. The output of the capacitance measurement circuit is subsequently monitored for 120 mins. Any leakage of water into the chamber region should lead to an increase in the effective dielectric constant between the sense electrode and diaphragm, and therefore, an increase in the capacitance. There is no detectable change in the output of the capacitance measurement circuit, which suggests that the epoxy film is watertight. The pressure equilibration potential of the ice detection sensor is also examined. While monitoring the output of the measurement circuit, the sensor package is thermally cycled between -20°C and 50°C using the heat pump. In a sealed chamber, this temperature change should cause pressure variations inside the chamber, which, in turn, should lead to diaphragm deformation. However, there is no detectable change in the capacitance between the membrane and the sense electrode, which indicates that there is no pressure change during thermal cycling. From these

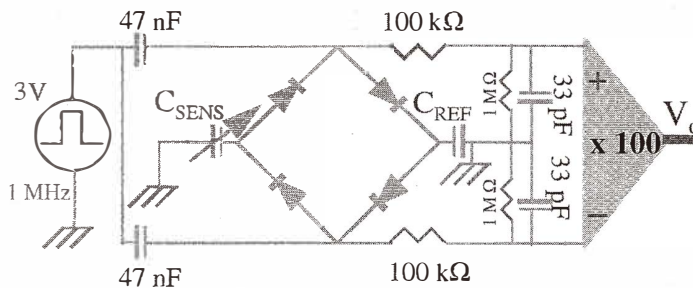


Fig. 8. Schematic layout of capacitance measurement circuit connected to the sense electrode (C_{SENS}). The amplified output, V_o , increases with $\Delta C = C_{\text{REF}} - C_{\text{SENS}}$. The minimum differential capacitance measurable is 0.2 pF.

observations, it appears that the epoxy seal prevents moisture seepage into the chamber region, but does not provide an airtight seal. The reason for this effect is not clear, but possible reasons might include microscopic pores in the epoxy film and/or defects in the boundary regions of the epoxy-ceramic and epoxy-silicon interfaces. Although the sealing qualities of the epoxy film worked to our advantage, it should be pointed out that additional investigation would be required to ensure the long-term reliability prior to mass production of the ice detection sensors.

The microfabricated sensor is then tested to determine its feasibility for ice detection. Using a micropipette, a droplet of deionized (DI) water is deposited on the diaphragm of the sensor. The thermoelectric cooler is turned on to cool and freeze the droplet. Next, a dc voltage is applied to the actuation electrode until the capacitance measurement circuit registers a change of ΔC_{MIN} . Figure 9 presents a graph of this minimum actuation voltage as functions of ice and water film thickness, which is estimated from knowledge of droplet volume and geometry. The minimum diaphragm actuation voltage increases from 30 V for the ice/water-free sensor to 96 V when covered with a 1.3-mm-thick ice film at -10°C . In contrast, the presence of water on the diaphragm and the sensor package has negligible effect on the minimum actuation voltage, which remains almost constant for different thicknesses of water films measured at 25°C . There is no observed change in the minimum actuation voltage upon cooling the ice/water-free sensor from 25°C to -10°C . These results indicate that the ice detection sensor system can successfully discriminate between ice and water films thicker than approximately 0.5 mm. It should be noted that a

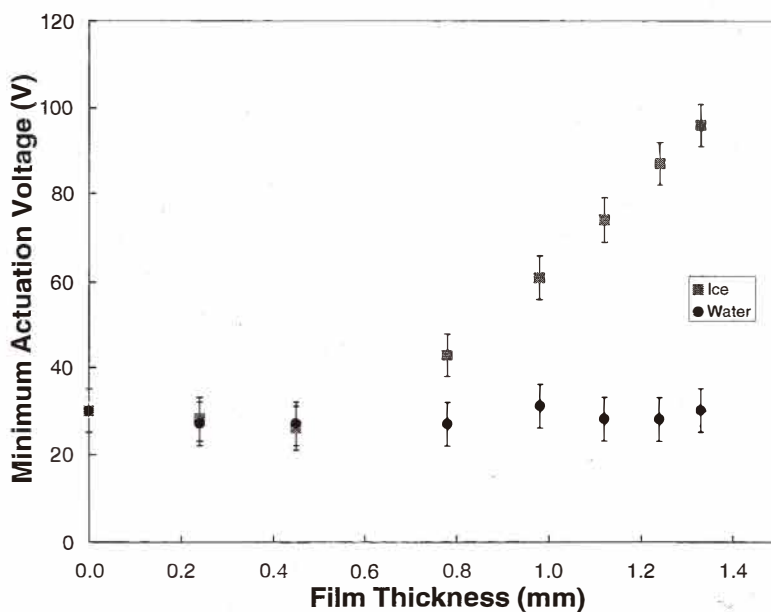


Fig. 9. Minimum diaphragm actuation voltage versus ice/water film thickness. The presence of water does not measurably affect the effective diaphragm stiffness.

sensor system based on an unbuckled diaphragm would enable the detection of even thinner ice films, as suggested by the FEA model.

Figure 10 presents an optical micrograph of ice formation on an aluminum substrate at -5°C . The water droplet has frozen into a clear sheet of ice which exhibits excellent adhesion to the underlying substrate, as determined by the “scratch” method.⁽¹³⁾ This evidence of strong adhesion explains our experimental observation of increasing actuation voltage, and hence the effective diaphragm stiffness, with growing ice thickness. The effect of frost on the ice detection system is investigated by cooling the sensor down to -10°C in an ambient with 80% relative humidity. As in the case of water films, the presence of frost, up to 3 mm thick, has no measurable effect on the minimum diaphragm actuation voltage. Figure 11 presents optical photographs of frost formation on an aluminum substrate at -8°C . The frost layer is composed of discrete ice crystals which are loosely arranged in a columnarlike structure. Also, the adhesion of frost to the underlying substrate tends to be relatively poor, which indicates the negligible effect of frost accumulation on the effective diaphragm stiffness.

Dynamic testing of the ice detection sensor is performed using a 30 Vrms, 1 Hz actuation signal with a droplet of DI water on the diaphragm. Two possible sensor actuation modes are tested: continuous and intermittent drive. In the continuous drive mode, ac actuation is applied at 25°C , and the continuously vibrating diaphragm is thermoelectrically cooled to -10°C . The capacitance change is measured periodically, while the water layer cools and turns into ice on the diaphragm. In the intermittent drive mode, the diaphragm is vibrated only at set temperature points during cooling. After measurement at a given set temperature, the actuation signal is switched off until the next

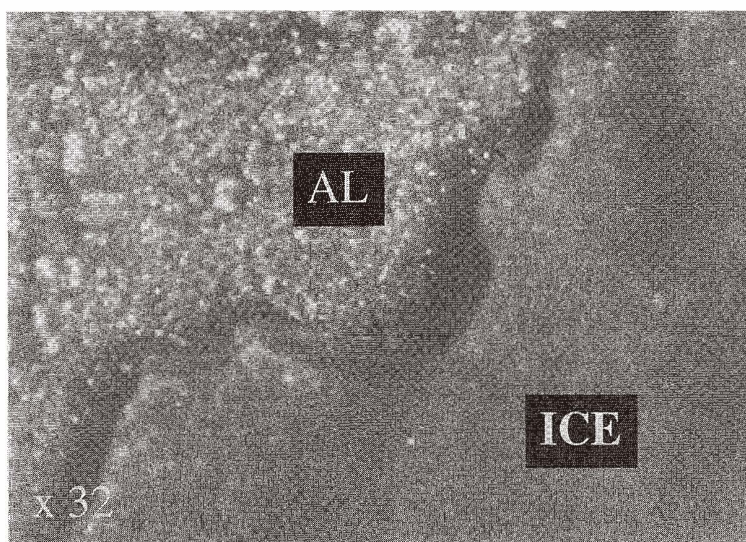


Fig. 10. Plan view micrograph showing clear ice formation at -5°C .

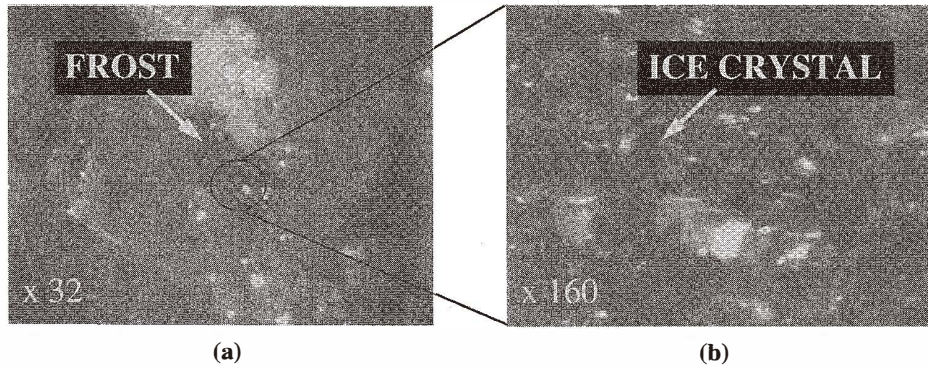


Fig. 11. Optical photographs (a): frost formation on an aluminum substrate at -8°C ; and (b) close-up showing discrete ice crystals arranged in a columnar-like structure.

set temperature is reached. Figure 12 presents graphs of the relative capacitance change of the diaphragm as a function of temperature for the different operational modes and ice thicknesses. For a given thickness of ice (0.6 mm), the continuous mode operation exhibits greater capacitance change than the intermittent mode. This observation suggests that the adhesion of ice to silicon is greater for the intermittently vibrating diaphragm. Consequently, the effective stiffness of the ice-covered diaphragm in the intermittent mode is greater, leading to a lower relative center displacement, and hence, capacitive change. As expected, thicker (0.8 mm) layers of ice lead to larger effective diaphragm stiffness, and therefore, smaller capacitance changes.

5. Conclusion

The feasibility of microfabricated, capacitive, diaphragm-type sensors for the detection of ice thickness is demonstrated. FEA results show that diaphragm deflection is affected by the stiffening effect of ice to a greater extent than by the weight of ice. Furthermore, the presence of either water or frost does not affect the effective diaphragm stiffness. In order to eliminate inaccuracies due to pressure fluctuations, the sensor design incorporates air-release channels to equalize pressure on both sides of the diaphragm. Device fabrication is accomplished by bulk micromachining and wafer bonding of glass and silicon substrates using a two-mask process. Prior to testing, the diaphragm chamber region is epoxy-sealed to prevent moisture seepage from the ambient and corresponding measurement error. By operating the diaphragm in the stiffness-sensitive mode, the sensor can discriminate between ice and water films. The sensor is tested on a thermoelectric cooler using a custom-built, high-sensitivity, differential capacitance measurement circuit. Calibration experiments reveal that the miniature ice detection sensor system can distinctly sense ice and water films between approximately 0.5–1.5 mm thick. Finally, dynamic sensor testing results indicate that the adhesion of ice to silicon is greater for the intermittently driven, rather than continuously vibrating, diaphragm.

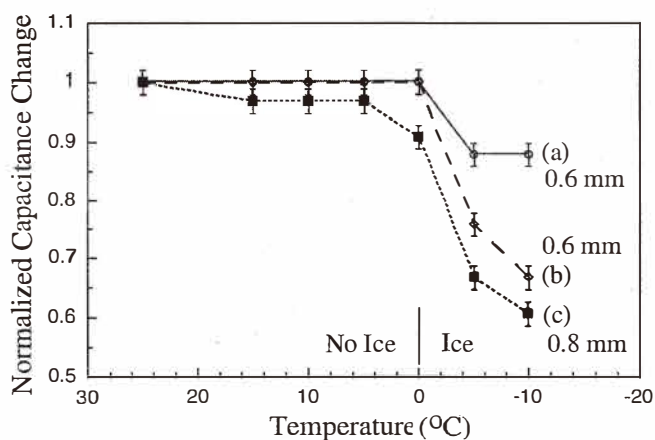


Fig. 12. Capacitance change of the diaphragm versus temperature for two different operational modes and ice film thicknesses: (a) continuous drive, 0.6-mm-thick ice layer; (b) intermittent drive, 0.6-mm-thick ice layer; and (c) intermittent drive, 0.8-mm-thick ice layer.

Acknowledgment

This work was supported by the Army Research Office under a Multidisciplinary Research Initiative, Grant No. DAAH04-95-10097.

References

- 1 B. B Stankov and A. J Bedard, Jr: *Journal of Aircraft* **31** (1994) 79.
- 2 D. P. Jensen and D. J. Moore: 8th Annual Natl. Conf. Env. Effects on Aircraft and Prop. Syst. (Bordentown, NJ, 1968).
- 3 R. J. Ranaudo, J. G. Batterson, A. L. Reehorst, T. H. Bond and T. M. O'Mara: *Journal of Aircraft* **28** (1991) 193.
- 4 A. Heinrich, et al.: *Aircraft Icing Handbook*, FAA Technical Center Publication, Atlantic City, NJ.
- 5 R. Freely: *Sensors* **11** (1994) 28.
- 6 R. G. DeAnna, M. Mehregany and S. Roy: Conf. Smart Struc. and MEMS, SPIE Symp. on Smart Struc. and Mat. (SPIE, San Diego, CA, 1997).
- 7 S. Roy, R.G. DeAnna, A. Izad and M. Mehregany: Proceedings of the IEEE MEMS Workshop (IEEE, Heidelberg, Germany, 1998) p. 75.
- 8 K. E. Petersen: Proceedings of the IEEE **70** (1982) 420.
- 9 R. J. Scavuzzo and M. L. Chu: NASA Contractor Report 179580 (1987).
- 10 F. Maseeh and S. D. Senturia: *Sensors and Actuators A-Physical* **23** (1990) 861.
- 11 X. Ding and W. H. Ko: Proceedings of the International Conference on Solid State Sensors and Actuators (IEEE, San Francisco, CA, 1991) p. 201.
- 12 V. Ziebart, O. Paul, U. Munch, J. Schwizer and H. Baltes: *Journal of Microelectromechanical Systems* **7** (1998) 320.
- 13 S. Roy, S. Furukawa and M. Mehregany: *Journal of The Electrochemical Society* **144** (1997) 3589.